KLOE Note 216

Measurement of the Radiative K^0_{e3} Branching Ratio and Direct Emission contribution in Semileptonic Decay $K_L \to \pi^{\pm} e^{\mp} \nu(\gamma)$

M. Antonelli, M. Dreucci, C. Gatti

Abstract

The study of radiative K_L decays offers the possibility to obtain informations on the kaon structure and the opportunity to test theories describing hadron interactions and decays, like chiral perturbation theory (ChPT). Two different components contribute to the photon emission, the inner bremsstrahlung (IB) and the direct emission (DE). The latter describes photon radiation from intermediate hadronic states, giving in this way new information. The KLOE experiment offers the possibility to perform precision measurements because of the K_L tagging. In fact, in the DAΦNE ϕ factory the K_L presence is tagged by the presence of a K_S decay, such as $K_S \to \pi^+\pi^-$. At the same time the K_S and ϕ momenta measurement allow to evaluate K_L momentum with good precision. KLOE, using $1/5^{th}$ of the full data sample, corresponding to about $9,000$ signal events, measured for the first time the DE contribution to $K^0_{e3\gamma}$. We find a 1.2σ significance level for the DE contribution, $\langle X \rangle = -2.3 \pm 1.3(stat) \pm 1.4(syst)$. We also measured the branching ratio of $K^0_{e3\gamma}$ with respect to the inclusive $K^0_{e3(\gamma)}$ events: R= BR($K^0_{e3\gamma}; E^*_\gamma > 30\,\mathrm{MeV}, \theta^*_\gamma > 20°$)/BR($K^0_{e3(\gamma)}$) $= (924 \pm 23 \pm 16) \times 10^{-5}$.

DRAFT 0 *12 September 2007*

1 Introduction

In the $K^0_{e3\gamma}$ decay, the IB component is much greater than the DE one, due also to the smallness of the electron mass. Infact the $K^0_{e3\gamma}$ amplitude in the kaon reference frame has infrared singularity for both $E^*_\gamma \to 0$ and $\theta^*_\gamma \to 0$ (photon angle *w.r.t.* lepton), for a null electron mass. Manly for historical reasons [1], the applied *standard cuts* to compare results are $E^*_\gamma > 30\,\mathrm{MeV}$ and $\theta^*_\gamma > 20°$. We define R as

$$R = \frac{\mathrm{BR}(K^0_{e3\gamma}; E^*_\gamma > 30\,\mathrm{MeV}, \theta^*_\gamma > 20°)}{\mathrm{BR}(K^0_{e3(\gamma)})} \tag{1}$$

With these cuts the theoretical predictions for R range between 0.95×10^{-2} and 0.97×10^{-2} [2]. The DE contribution in any case is expected to be less than 1% of IB. Up to now the experimental values of R are in marginal disagreement with theoretical predictions, so that new measurements are welcome.

This note is organized in the following manner:

- KLOE detector
- Inclusive $K^0_{e3(\gamma)}$ sample selection
- Efficiency evaluation
- Radiative subsample selection
- Control sample: calibrations and efficiency correction
- Monte Carlo reliability
- Fit result
- Systematics
- R result and DE contribution
- Comparison with the 2001 KTeV measurement
- Conclusion

2 The KLOE detector

The KLOE detector consists of a large cylindrical drift chamber (DC), surrounded by a lead scintillating-fiber electromagnetic calorimeter (EMC). A superconducting coil around the calorimeter provides a 0.52 T field. The drift chamber [3] is 4 m in diameter and 3.3 m long. The momentum resolution is $\sigma_{p_\perp}/p_\perp \approx 0.4\%$. Two-track vertices are reconstructed with a spatial resolution of ~ 3 mm. The calorimeter [4] is divided into a barrel and two endcaps. It covers 98% of the solid angle. Cells close in time and space are grouped into calorimeter clusters. The energy and time resolutions are $\sigma_E/E = 5.7\%/\sqrt{E\ (\mathrm{GeV})}$ and $\sigma_T = 57\ \mathrm{ps}/\sqrt{E\ (\mathrm{GeV})} \oplus 100\ \mathrm{ps}$, respectively.

The KLOE trigger [5] uses calorimeter and chamber information. For this analysis, only the calorimeter signals are used. Two energy deposits above threshold ($E > 50$ MeV for the barrel and $E > 150$ MeV for the endcaps) are required. Recognition and rejection of cosmic-ray events is also performed at the trigger level. Events with two energy deposits above a 30 MeV threshold in the outermost calorimeter plane are rejected. The 328 pb^{-1} of data used in this analysis, taken in 2001 and 2002, are divided in 14 periods of about 25 pb^{-1}/period. For each data period we have a corresponding period simulated with Monte Carlo with about the same statistic.

3 Sample selection

The sample selection procedes via the tagging, the K_L decay track candidates search and vertexing, the track to cluster association (TCA) and the particle identification by time of flight (TOF).

3.1 Tagging

K_L decays events are identified by the presence of a $K_S \to \pi^+\pi^-$ decay. We require a vertex with two tracks of opposite curvature with origins within a cylindrical FV of radius r_{xy} <10 cm and lenght Δz <20 cm, centered in the collision region, $\mathbf{x}_\phi$, being this last determined for each run using Bhabha events. The invariant mass computed from the track momenta, in the hypothesis of pion mass, must be within 5 MeV of K_S mass. Moreover, the total momenta evaluated from the two tracks must be within 10 MeV of the value expected from a two-body ϕ decay kinematics and the value of $\mathbf{p}_\phi$, as determined from Bhabha events. If more than one vertex satisfies these criteria, that closest to the nominal ϕ vertex is identified as the K_S. The K_L momentum, p_{K_L}, is obtained from the kinematics of the $\phi \to K_S K_L$ decay, using the K_S direction reconstructed from the measured momenta of the decay tracks and the known value of $\mathbf{p}_\phi$, *i.e.* $\mathbf{p}_{K_L} = \mathbf{p}_\phi - \mathbf{p}_{K_S}$. The resolution is dominated by the beam-energy spread, and amounts to about 0.8 MeV/c. The K_L line of flight (*tagging line*) is constructed from the K_L momentum, and the position of the production vertex, $\mathbf{x}_\phi$. The value of the TAG efficiency obtained from Monte Carlo simulation is about 65%

3.2 Extrapolation of K_L Decay Tracks

All relevant tracks in the chamber, after removal of those from the K_S decay and their descendants, are extrapolated to their points of closest approach to the *tagging line*. For each track candidate, we evaluate the point of closest approach to the *tagging line*, $\mathbf{x}_\mathrm{c}$, and the distance of closest approach, d_c. The momentum $\mathbf{p}_\mathrm{c}$ of the track at $\mathbf{x}_\mathrm{c}$ and the extrapolation length, l_c, are also computed. Tracks satisfying $d_\mathrm{c} < a r_{xy} + b$, with $a = 0.03$

and $b = 3$ cm, and -20 cm $< l_c < 25$ cm are accepted as K_L decay products, being r_{xy} the distance of the vertex from the interaction point (IP) in the transverse plane. For each sign of charge we consider as associated to the K_L decay the track with the smallest value of d_c. Starting from these track candidates a vertex is reconstructed. The events are retained if the vertex is in the fiducial volume $35 < r_{xy} < 150$ cm and $|z| < 120$ cm. The combined tracking and vertexing efficiency for K^0_{e3} is about 54%.

3.3 Extrapolation of the tracks to the calorimeter

For the purposes of track-to-cluster association (TCA), we define two quantities related to the distance between the track, extrapolated at the entry point of the calorimeter, and the closest cluster: $\mathrm{d_{TC}}$, the distance from the extrapolated entry point on the calorimeter to the cluster centroid and $\mathrm{d_{tc\perp}}$, the component of this distance in the plane transverse to the momentum of the track at the impact position. The distribution of this last variable is shown in Fig. 1 for data and Monte Carlo. We only consider clusters with $\mathrm{d_{tc\perp}} < 30$ cm. If there is more than one cluster candidate, we retain the cluster for which $\mathrm{d_{tc\perp}}$ is smaller.

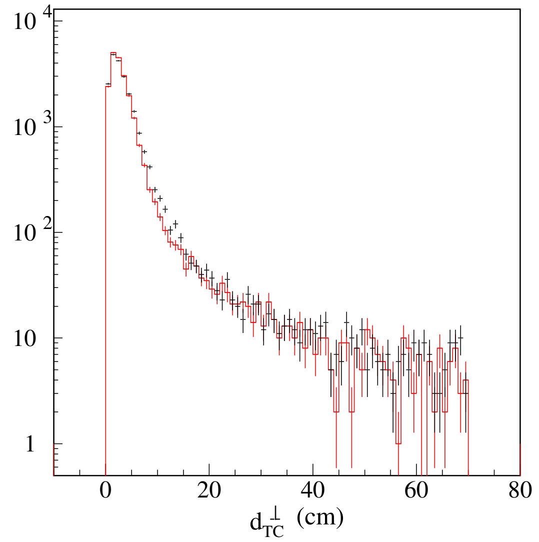

Fig. 1. Plot of $\mathrm{d_{tc\perp}}$ in barrel ECAL for Monte Carlo (solid line) and Data(dots).

3.4 Kinematic based event selection

To remove background from $K_L \to \pi^+\pi^-\pi^0$ and $K_L \to \pi^+\pi^-$ with minimal efficiency loss we apply a set of loose kinematic cuts: assuming the two tracks belong to pions, we require

$$E^2_{miss} - p^2_{miss} - m^2_{\pi^0} < -5000 \ \mathrm{MeV}^2 \tag{2}$$

and

$$\sqrt{E_{miss}^2 + p_{miss}^2} > 10\,\text{MeV}, \tag{3}$$

respectively, for $K_L \to \pi^+\pi^-\pi^0$ and $K_L \to \pi^+\pi^-$ events. E_{miss} and p_{miss} are the missing energy and momentum. The distributions of these variables obtained from Monte Carlo simulation are shown below in Fig. 2 for the signal and for the background. After these cuts the efficiency remains close to 1 while the background rejection is about 90%. Background from $K_L \to \pi\mu\nu$

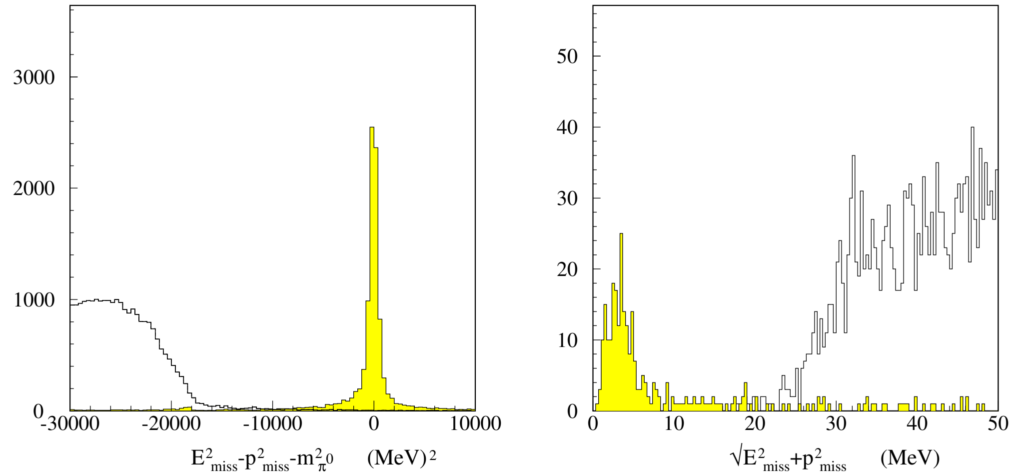

(a) $K_L \to \pi^+\pi^-\pi^0$ events (b) $K_L \to \pi^+\pi^-$ events

Fig. 2. Monte Carlo: kinematic cuts for background. In both cases we assume the pion mass for each track. Signal solid, background filled.

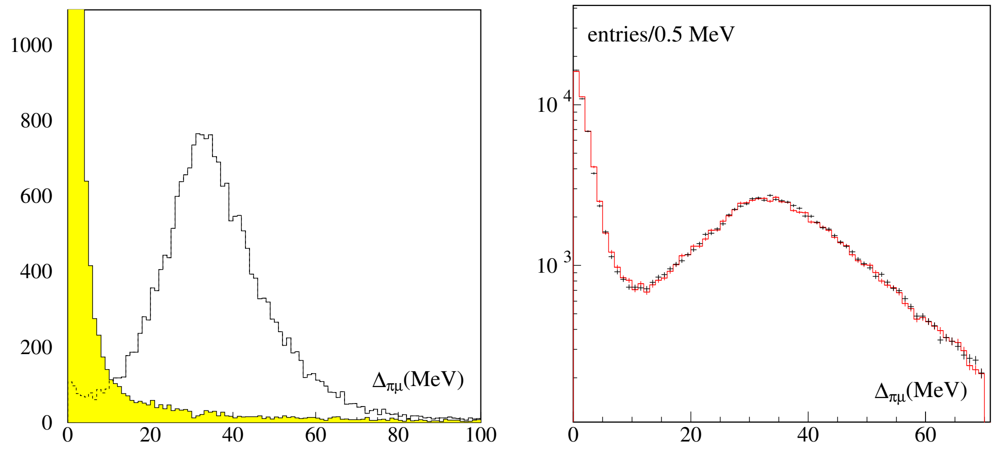

(a) Monte Carlo (b) Data-Mc comparison

Fig. 3. (a) Monte Carlo: $\Delta_{\pi\mu}$ distribution for $K_L \to \pi\mu\nu$ background (filled) and signal (solid). (b) Data-MC comparison for $K_L \to \pi^\pm\ell^\mp\nu$ events after the kinematical cuts

has been drastically reduced using $\Delta_{\pi\mu}$, the lesser between $|E_{miss} - p_{miss}|$ in the two hypothesis, $\pi\mu$ or $\mu\pi$. The distribution of $\Delta_{\pi\mu}$ obtained from Monte Carlo is shown in Fig. 3 for signal and background. We retain events only if $\Delta_{\pi\mu} > 10\,\mathrm{MeV}$. The use of $\pi\mu$ hypothesis is more effective than the alternative πe hypothesis: in the former we have an efficiency of $\sim 97\%$ with a contamination of $\sim 10\%$, in the latter an efficiency of $\sim 85\%$ and a contamination of $\sim 6.5\%$. The efficiency of all kinematical cuts is about 96%.

3.5 Event Selection using Time of flight

The kinematic event selection does not remove the background from $K_L \to \pi e \nu$ with wrong charge assignement and from $K_L \to \pi \mu \nu$ decay at the desired level. The total background contamination after kinematic cuts is about $\sim 12\%$, mainly due to $K_L \to \pi\mu\nu$. To further reduce thise contamination we make use of the time of flight information. We define for the i^{th} track outcoming from the K_L vertex and associated to a cluster:

$$\Delta t_i = t_{\mathrm{cl}} - t_{\mathrm{exp}}, \qquad (i = \pi^+, \pi^-, e^+, e^-) \tag{4}$$

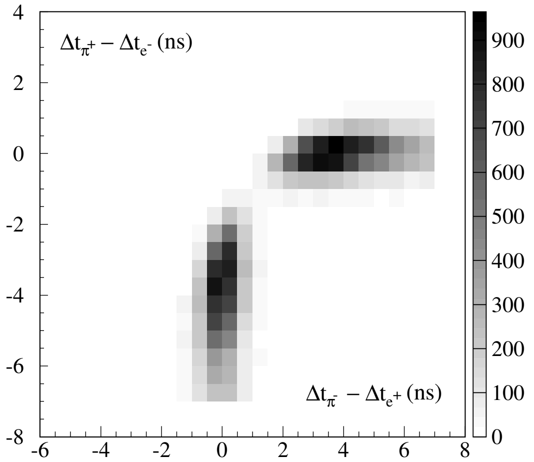

Fig. 4. Distribution of $\Delta t_{\pi^+} - \Delta t_{e^-}$ vs $\Delta t_{\pi^-} - \Delta t_{e^+}$ for Monte Carlo signal events

in which t_{cl} is the cluster time and t_{exp} is the expected time of flight, evaluated according to a well defined mass hypothesis. In the evaluation of t_{exp} we also include the time from the impact point to the cluster centroid distribution as in [6]. An effective way to select the correct charge assignment, πe or $e\pi$, is obtained by choosing the lesser between $|\Delta t_{\pi^+} - \Delta t_{e^-}|$ and $|\Delta t_{\pi^-} - \Delta t_{e^+}|$. Fig. 4 shows infact a net separation for the two cases. After the charge assignment we consider the variables $\Delta t_\pi + \Delta t_e$ and $\Delta t_\pi - \Delta t_e$. The scatter plot of $\Delta t_\pi - \Delta t_e$ vs $\Delta t_\pi + \Delta t_e$ obtained from Monte Carlo simulation is shown in Fig. 5 for the signal and the background. The time resolutions are 0.5 ns and 0.4 ns for the pions and the electrons, respectively.

We apply a 2σ elliptic cut to select the signal (Fig. 5). The efficiency of this cut is about 70%. After the TOF cut we have a contamination of $\sim$0.7%,

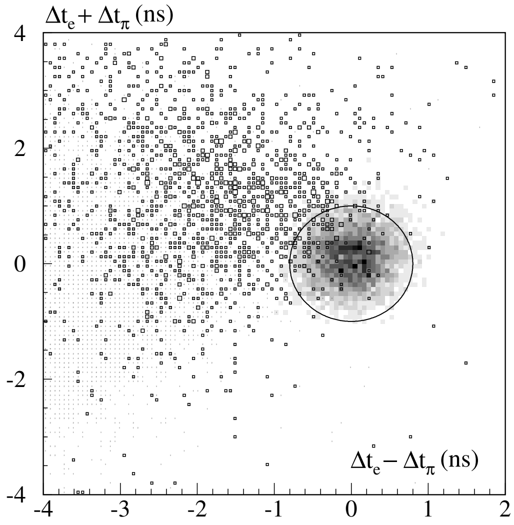

Fig. 5. Monte Carlo: $\Delta t_e + \Delta t_\pi$ versus $\Delta t_e - \Delta t_\pi$. Signal (gray scale), background from opposite sign (dot), background from $K_L \to \pi\mu\nu$ same sign (box).

almost entirely due to $K_L \to \pi\mu\nu$ decay.

4 Efficiency evaluation

The total efficiency:

$$\epsilon_{tot} = \epsilon_{rec}(E^*_\gamma) \times \epsilon_{kine}(E^*_\gamma) \times \epsilon_{tof}(E^*_\gamma) \tag{5}$$

is given by the product of reconstruction efficiency, $\epsilon_{rec}(E^*_\gamma)$, which includes the tagging, the tracking and the clustering requirements, times the kinematic event selection, $\epsilon_{kine}(E^*_\gamma)$, times the TOF event selection, $\epsilon_{tof}(E^*_\gamma)$. All reconstruction efficiencies are directly evaluated from data control samples and folded with the expected kinematic distributions from Monte Carlo. The efficiency for the kinematic and TOF event selections are evaluated from Monte Carlo where data driven corrections have been implemented.

4.1 Tagging efficiency

As mentioned in Sec.3 K_L decays events are identified by the presence of a $K_S \to \pi^+\pi^-$ decay. The TAG efficiency has been obtained from Monte Carlo simulation . Fig. 6 shows the TAG efficiency to be independent on photon energy. Its value is about 66%.

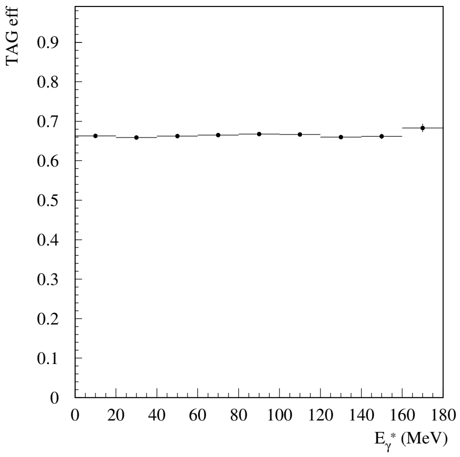

Fig. 6. Tagging efficiency from Monte Carlo simulation as a function of photon energy. Full statistic

4.2 Tracking and vertex efficiency

The tracking efficiency is determined by counting the number of events in which there is at least a K_L decay track and the number of events in which there are two decay tracks of opposite sign (see [7]). The data-MC difference in the single-to-double ratio is used to correct the MC estimate for the tracking efficiency. This correction is evaluated as a function of the track momentum using $K_L \to \pi^+\pi^-\pi^0$ and $K_L \to \pi^\pm e^\mp \nu$ events as control samples. In $K_L \to \pi^+\pi^-\pi^0$ events, the momentum of one decay track is calculated with a resolution of about 10 MeV using the two photons from the π^0 decay, the momentum of the other decay track and the K_L momentum. In order to obtain the correction for higher momentum tracks (above ~ 150 MeV), $K_L \to \pi^\pm e^\mp \nu$ decays are used, in which the electrons are identified by time of flight with a purity of $\sim$95%. The momentum of the second K_L track is evaluated from the missing energy with a resolution of about 30 MeV. To select $K_L \to \pi^+\pi^-\pi^0$ events, we require at least one K_L decay track and two photons from the π° decay. To reject background, cuts are applied on the two-photon invariant mass and on the times of flight of the photons.

The vertex efficiency is the ratio of the number of events with at least two K_L decay tracks of opposite charge that form a vertex to the number of events with at least two K_L decay tracks of opposite charge. As shown in Fig. 7, the vertex efficiency is close to 1, and the values obtained from Monte Carlo are in agreement with those from data to within 0.1%. The Monte Carlo combined efficiency for tracking and vertexing efficiency is shown in Fig. 8(a) as a function of the photon energy. The corresponding correction from control samples is shown in Fig.8(b).

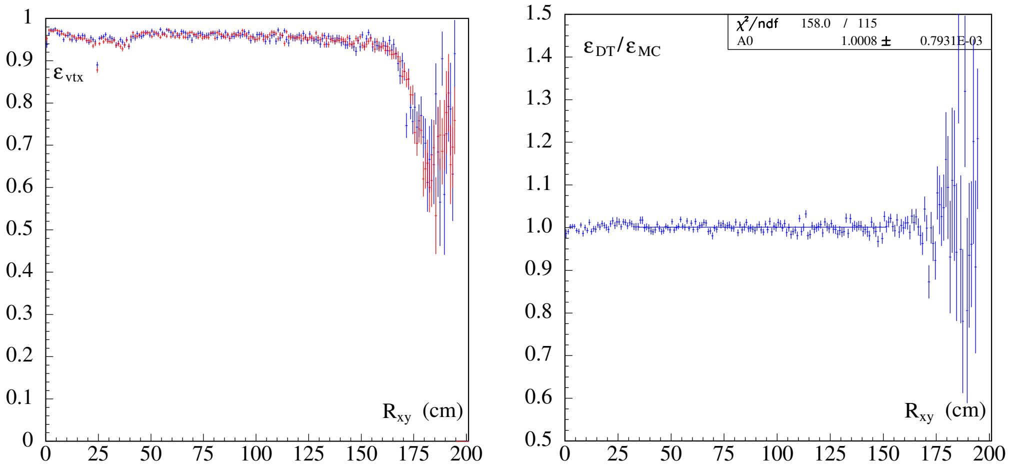

Fig. 7. Left: Vertex efficiency as a function of the transverse radius for data (blue) and Monte Carlo (red). Right: Data-Monte Carlo ratio of vertex efficiencies as a function of the transverse radius.

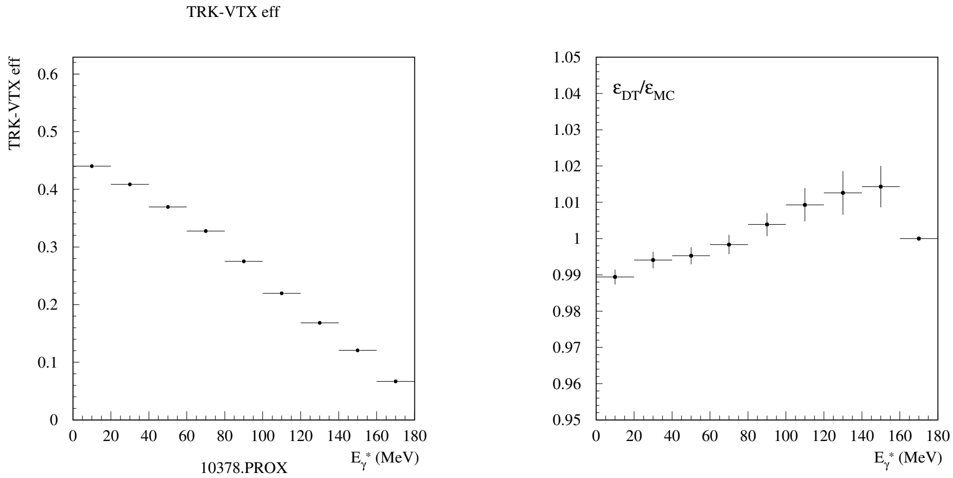

(a) (b)

Fig. 8. (a) Tracking and vertexing combined efficiency from Monte Carlo as a function of photon energy. (b) Correction to tracking and vertexing efficiency from control sample. Both plots refer to a single period

4.3 Track-to-cluster efficiency

The track-to-cluster efficiency has been evaluated from a pure sample of electrons and pions from $K^0_{e3(\gamma)}$ selected by means of kinematics and independent calorimeter informations. The data-MC ratio in the efficiency obtained from the control sample is used to correct the MC efficiency simulation. Kinematics select K^0_{e3} with a purity of about of 98%: $\Delta_{\pi e}$, the lesser between $|E_{miss} - p_{miss}|$ in the two hypothesis, πe or $e\pi$, is required to be smaller than 5 MeV (see Fig. 9). Then, $K_L \to \pi^+ e^- \overline{\nu}$ events are separated

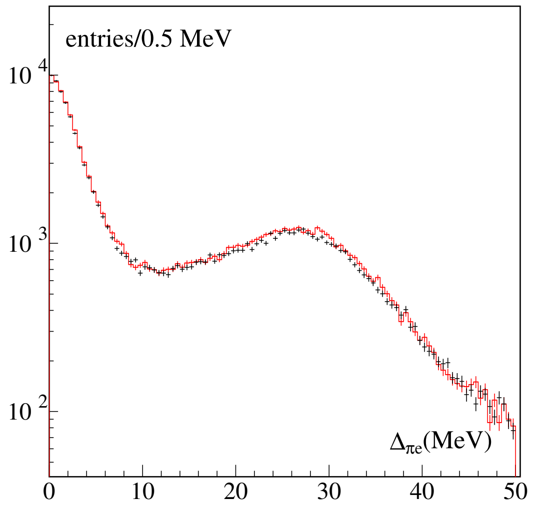

Fig. 9. Comparison Data-MC for $K^0_{e3(\gamma)}$ control sample: $\Delta_{\pi e}$ distribution for $K_L \to \pi^{\pm}\ell^{\mp}\nu$.

from $K_L \to \pi^- e^+ \nu$ events using the following variable:

$$y_{rec} = \frac{|M^2_\ell(e,\pi) - m^2_e|^{1.5} - |M^2_\ell(\pi,e) - m^2_e|^{1.5}}{max|M^2_\ell - m^2_e|^{1.5}} \tag{6}$$

in which $M^2_\ell(i,j)$ is the lepton invariant mass squared reconstructed with the two mass hypotheses, πe or $e\pi$, obtained from:

$$M^2_\ell = (p_K - p_\pi - p_{miss})^2$$

in which we assume a zero mass for neutrino. We have used different values for the exponent in Eq. 6: the value 1.5 maximizes separation according to MC. In Fig. 10 the distribution of this variable for signal and background is shown. We cut at $y_{rec} > 0.8$ (< -0.8) to select $K_L \to \pi^+ e^- \overline{\nu}$ ($K_L \to \pi^- e^+ \nu$). The selection of $e^{\pm}$ ($\pi^{\pm}$) events is finally reinforced by the TOF identification of the other track, for which a $|\Delta t_i| < 0.5$ ns is imposed. A purity of about 99.5% is obtainded after these requirements.

The contribution of the cluster and track extrapolation efficiencies to the track-to-cluster association efficiency have been studied individually. Both the cluster efficiency and track extrapolation efficiency have been studied as a function of the particle momenta, the K_L vertex position, impinging angle, and the cluster position (barrel or endcap). Only the dependence on the particle momentum and on the cluster position have been used for the cluster efficiency and the track extrapolation efficiency. The impact of this assumption has been studied by repeating the evaluation of the efficiency including other dependencies such as the K_L vertex position and the impinging angle. No significant dependancy on these variables has been observed.

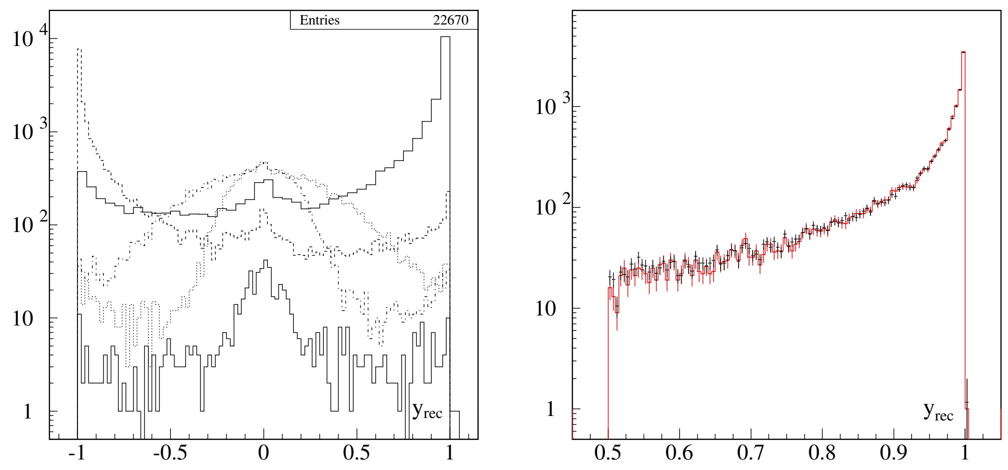

(a) (b)

Fig. 10. y_{rec} distribution. (a) Monte Carlo: signal (solid, high statistic) and all background sources (dashed plus solid low statistic); (b) Data-Monte Carlo comparison for signal taken from control sample

The efficiencies have been evaluated separately for the 14 run-periods both for data and Monte Carlo. A set of 168 particle momentum dependent efficiencies have been produced for data and Monte Carlo, corresponding to different particle type, $e^{\pm}$ and $\pi^{\pm}$, and to different detector type, barrel and endcap. The data Monte Carlo ratio of the efficiency measured on the control samples is used to correct the Monte Carlo evaluation.

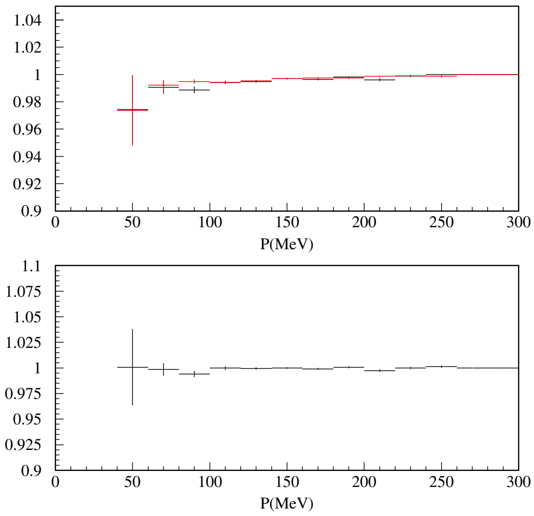

Fig. 11. Top: Cluster efficiency for electrons on the barrel from $K^0_{e3(\gamma)}$ control sample for data (black) and MC (red). Bottom: data Monte Carlo ratio. The plots refer to a single period.

For electrons and positrons the correction results to be small (Fig. 11), while for pions can be large as 30%, and it is different for π^- and π^+, (Fig. 12).

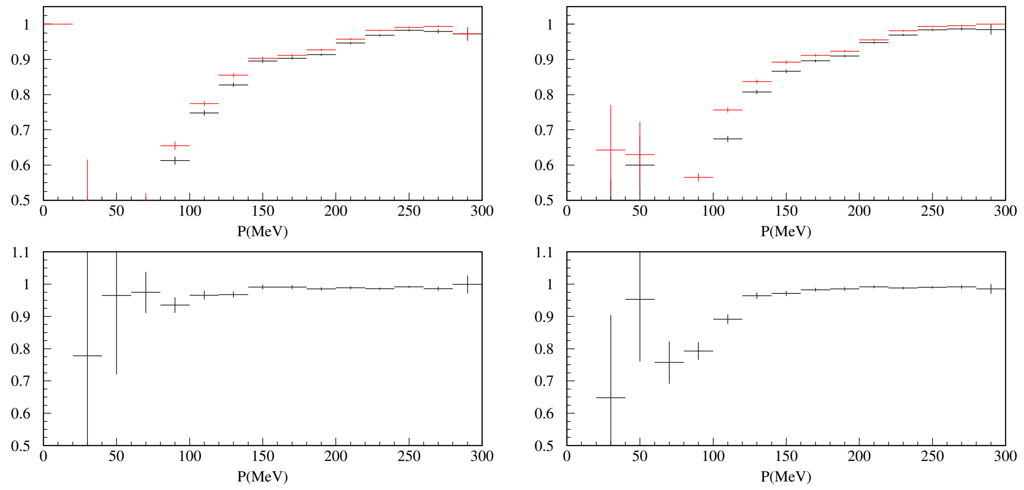

(a) (b)

Fig. 12. Top: Cluster efficiency from control sample for data (black) and Monte Carlo (red). Bottom: data Monte Carlo ratio. For π^- (a) and π^+ (b) The plots refer to a single period

4.4 TOF efficiency

TOF efficiency is taken from a Monte Carlo with corrections in the time response of the calorimeter taken from control samples [6]. The data and Monte Carlo distribution of Δt_e and Δt_π are shown in Fig. 13 for events selected as described in the previous section. The agreement is adequate for our purpose.

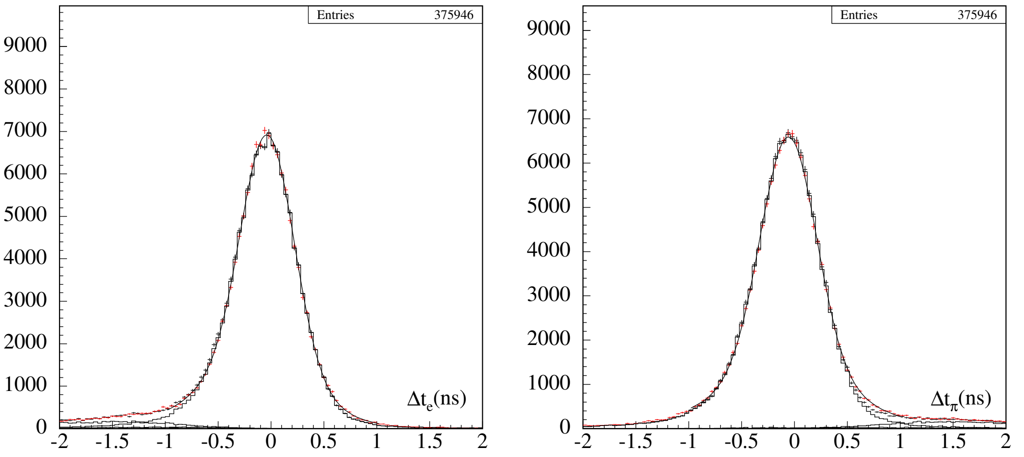

(a) (b)

Fig. 13. Δt_i for electron (a) and pion (b) for data (black) and Monte Carlo (red)

5 Radiative subsample selection

Our signal is a $K^0_{e3\gamma}$ event with $E^*_\gamma > 30\,\text{MeV}$ and $\theta^*_\gamma > 20°$ (*standard cut*). To select the $K^0_{e3\gamma}$ signal we look for a cluster not assigned to any track compatible in time with a photon originating from a point (neutral vertex, NV) close to the K_L charged vertex. We apply a $8\sigma_R$ cut on d_{NC}, the NV distance from the charged vertex position, being σ_R its resolution. In case of more than one photon candidate, we choose the closest to the K_L charged vertex.

To evaluate the photon energy we use only kinematic informations, *i.e.*, charged track momenta and photon cluster position. By solving Eq.7 below in the hypothesis of neutrino zero mass, being $\hat{u}$ the photon direction, we extract the photon energy with a resolution of $\sim$1 MeV. This resolution is a factor ~ 10 better than that obtained using the energy deposit information of calorimeter.

$$p_\nu = p_K - p_\pi - p_e - p_\gamma \quad ; \quad \mathbf{p}_\gamma = E_\gamma \hat{u} \tag{7}$$

In Fig. 14 is shown the selection efficiency for the signal as taken from Monte Carlo simulation. The main background contribution at low photon

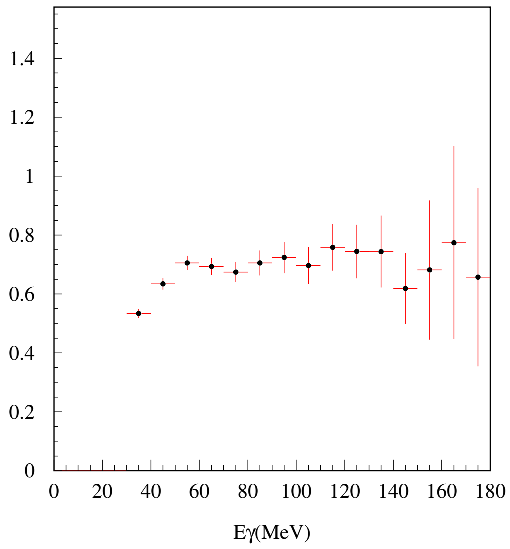

Fig. 14. Signal efficiency from Monte Carlo simulation. One period.

energy comes from $K^0_{e3\gamma}$ with an undetected soft-photon and where a cluster from accidentals has been wrongly associated. We remove these accidentals by cutting in the scatter plot plane $E_{CLU} - E^{lab}_\gamma$ vs E_{CLU}, as shown in Fig. 15. E^{lab}_γ is the reconstructed photon energy in the laboratory system and E_{CLU} the energy of the associated cluster. In Fig. 15(b) is shown the distribution of the distance between the electron-cluster and the photon-cluster. Before applying the cut (top) Monte Carlo simulation indicates a ratio accidentals/signals ~ 1.7 and a strong disagreement with respect to data at small distances. After the cut (bottom) this ratio becomes ~ 0.2 and the agreement is very good, with only a $\sim$6% loss in signal efficiency.

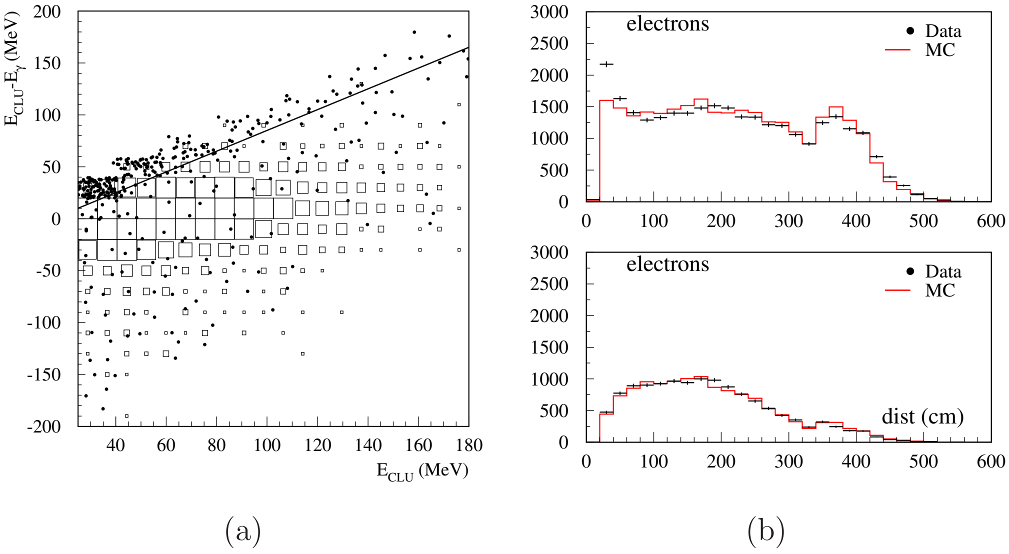

Fig. 15. (a) Sliding cut to remove accidentals. (b) Distance of γ-cluster from electron-cluster in Data and Monte Carlo before (top) and after (bottom) cut.

5.1 *Background rejection*

Background from $K_L \to \pi^+\pi^-\pi^0$ and $K_L \to \pi\mu\nu$ events after signal selection is at level of $\sim 4.2\%$ and $\sim 2.5\%$, respectively. As shown in Fig. 22 this background overlaps with the physically interesting DE contribution, so we need to remove it as much as possible. This can be done only using a particle identification (PID) procedure.

To remove $K_L \to \pi^+\pi^-\pi^0$ events we make use of a Neural Network (NN) trained with the control sample described in the next section. The input variables for this NN are: the reconstructed photon energy and angle (*w.r.t.* lepton), the energy of the tracks, the missing momentum and $M^2_{\gamma-\nu}$, the invariant mass of photon-neutrino pair. In Fig. 16(a) is shown the distribution of this NN output for data and Monte Carlo

For $K_L \to \pi\mu\nu$ events is possible to make a sufficient separation from $K_L \to \pi^\pm e^\mp \nu$ only by using calorimetric informations. This NN has been trained with a control sample of K^0_{e3} and $K^0_{\mu 3}$ events selected with tight kinematic cuts. Input variables are the track momenta, the calorimetric energy deposit and the centroid position. The purity is about $\sim 95\%$. In Fig. 16(b) is shown the distribution of this NN output for data and Monte Carlo

Requiring the output value of these NNs to be greater than 0.2 we have a background reduction from $4.2\% \to 0.4\%$ and from $2.5\% \to 1.4\%$, respectively for $K_L \to \pi^+\pi^-\pi^0$ and $K_L \to \pi\mu\nu$, with a tolerable loss in the efficiency of our signal (10%).

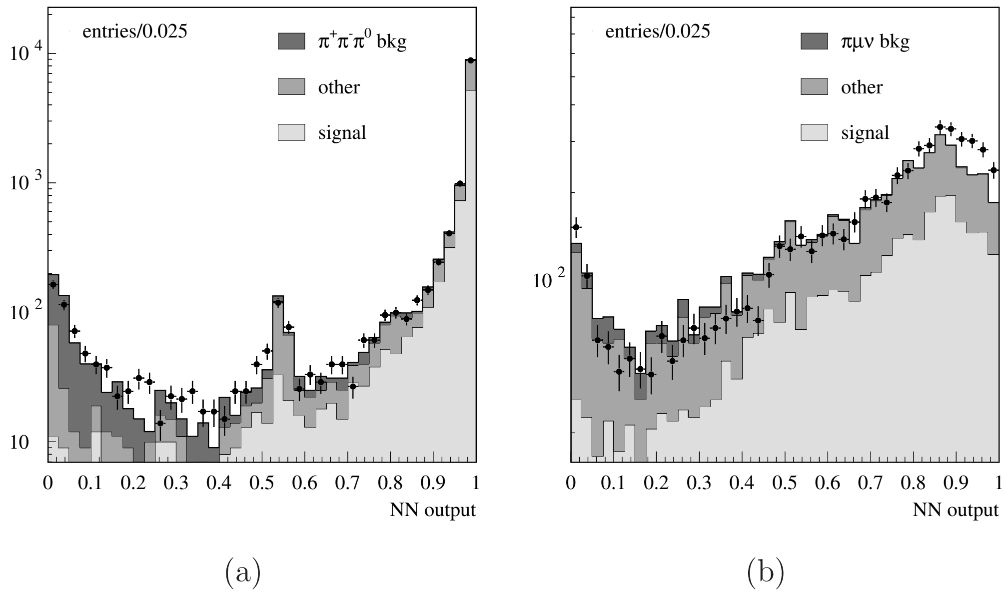

Fig. 16. NN output distribution for data (dot) and Monte Carlo (solid). (a) NN for $K_L \to \pi^+\pi^-\pi^0$ rejection; (b) NN for $K_L \to \pi\mu\nu$ rejection (only a charge)

6 Control sample

To check the Data-Monte Carlo agreement, to calibrate the Monte Carlo position of NV and correct photon selection efficiency we use as a control sample events from the decays $K_L \to \pi^+\pi^-\pi^0$. To select these events we apply a tight kinematic cut in the variable $E^2_{miss} - p^2_{miss} - m^2_{\pi^0}$ in the hypothesis of two pion tracks (see Fig. 2). Further, we require the presence of a cluster (E>60 MeV) not associated to any track, corresponding to one of the two photons from π^0 decay. This high energy photon is used to tag the presence of the second photon. We select about 350,000 $K_L \to \pi^+\pi^-\pi^0$ events with a purity of 99.8%.

6.1 Photon energy resolution

As a first check of Data-Monte Carlo agreement we want to compare the energy resolution of the photons. This can be done because in this control sample we estimate the energy of the second photon (the tagged photon) exactly in the same way (Eq. 8) than in our $K^0_{e3\gamma}$ signal selection: there we do not detect the neutrino, here we can ignore the hard photon (the tagging photon). In fact Eq.8 and Eq. 7 are identical with respect to *r.h.s.*. After squaring also *l.h.s.* becomes identical (*i.e.*, zero) and the (second) photon energy is extracted.

$$p_{\gamma-hard} = p_K - p_\pi - p_\pi - p_\gamma \quad ; \quad \mathbf{p}_\gamma = E_\gamma \hat{u} \tag{8}$$

The energy resolution of this photon is evaluated with respect to a value computed in a more accurate using the complete hard photon informations

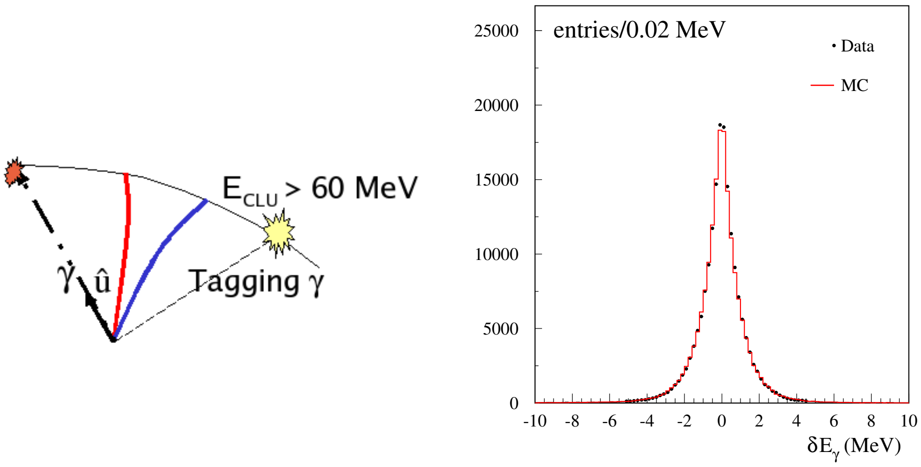

(a) (b)

Fig. 17. (a) Control sample selection. (b) Photon energy resolution

and closing in this way the kinematic. In Fig. 17(b) the residual is shown for data and Monte Carlo and a good agreement results.

6.2 Calibrations

In the $K^0_{e3\gamma}$ signal selection we search for a photon originating within a defined distance from the charged vertex position. We use the control sample from $K_L \to \pi^+\pi^-\pi^0$ to evaluate the distance of the neutral vertex from the charged vertex, d_{NC}, and its resolution. In Fig. 18 is shown the distribution of d_{NC} and its resolution as a function of the transverse distance r_{xy} as taken from $K_L \to \pi^+\pi^-\pi^0$ control sample. In Fig. 19(a) is shown the distribution of the neutral vertex distance from charged vertex position, d_{NC}, after calibration. The $K^0_{e3\gamma}$ signal selection also requires a cut (Fig. 15) to remove fake associations due to the accidentals. This cut makes use of cluster energy, so we need also to check the calorimeter energy response. The Monte Carlo energy response is about $\sim$2 MeV lower than data. This bias is with a good approximation independent on the energy. In Fig. 19(b) is shown the distribution of the calorimeter response after calibration.

6.3 Efficiency correction

Using this tagging technique we evaluate the efficiency from data and Monte Carlo in the control sample and use their ratio to correct photon efficiency from Monte Carlo simulation. The correction is of the order of a few percent. This correction is shown in Fig. 20(a) as a funtion of the run period. In the Fig. 20(b) is shown this correction as a function of photon energy.

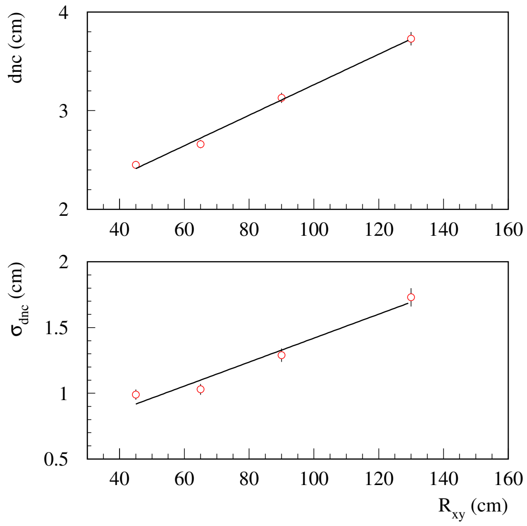

Fig. 18. Distribution from $K_L \to \pi^+\pi^-\pi^0$ control sample. Neutral vertex-charged vertex distance, d_{NC} (top). d_{NC} resolution (bottom)

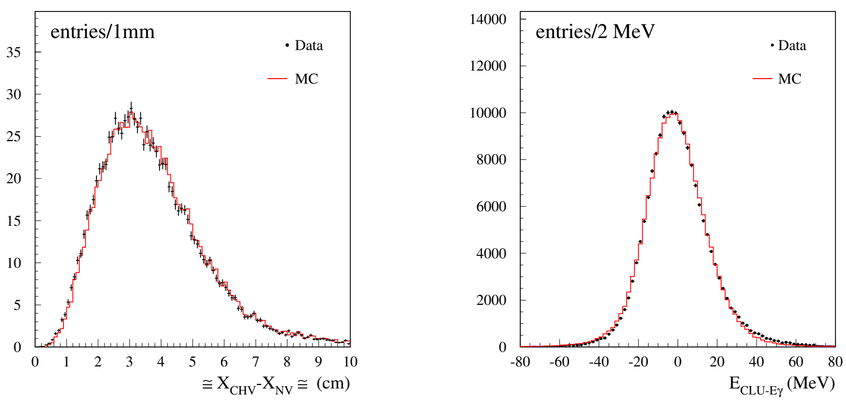

(a) (b)

Fig. 19. After calibration: (a) NV-CH distance distribution, d_{NC}, in the central part of DC (b) $E_{CLU} - E_{\gamma}^{lab}$ distribution

7 Monte Carlo reliability

We know that KLOE Monte Carlo [8] for $K^0_{e3\gamma}$ radiative events, after integration in the space phase, has an accuracy level of a few % in describing the photon spectrum, an appropriate level for many KLOE measurements. Unfortunately, this accuracy level is of the same order of DE contribution, which is 1% of IB one. For this reason we use a stand alone Monte Carlo production (*Kubis* Monte Carlo) based on a code provided by one of the autors of Ref. [2], which implements their $\mathcal{O}(p^6)$ calculation. We generate several millions of events both for IB and DE component. A comparison of these Monte Carlos confirms this discrepancy level. From the point of

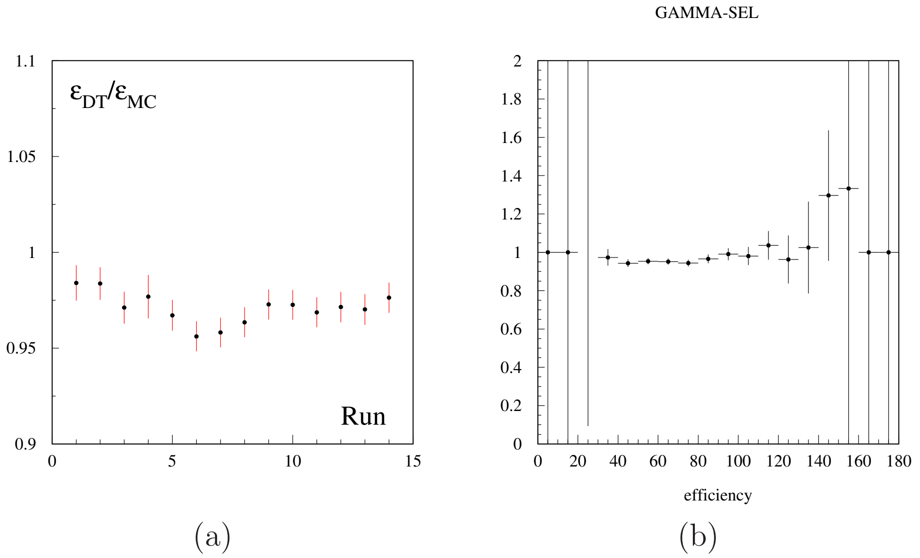

Fig. 20. (a) Efficiency correction as a function of run period (b) Shape efficiency correction

view of R measurement this discrepancy could introduce a $\sim$1% error on R. On the other side, a fit counting procedure based on a 1%-biased IB distribution could introduce up to a 100% error counting in $K^0_{e3\gamma}$ from DE events. For this reason we use the *Kubis* Monte Carlo to fit both IB and DE

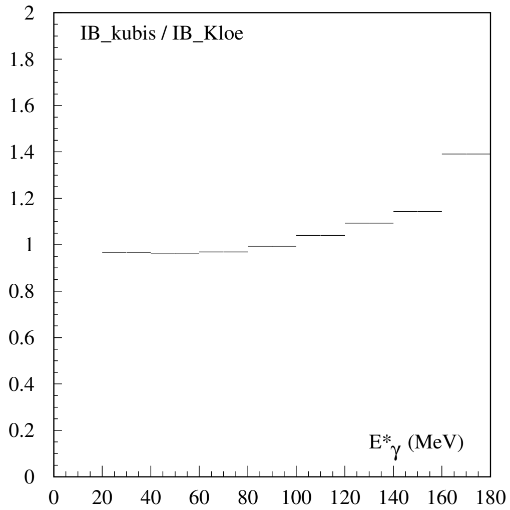

Fig. 21. Ratio Kubis/Kloe Monte Carlo for IB distribution as a funcion of photon energy in kaon rest frame

spectra. This Monte Carlo is folded with the KLOE reconstruction directly. Event by event infact, for each selected photon, we know the true E^*_γ and θ^*_γ values from which we evaluate the ratio $r_{IB} = MC^{Kubis}_{IB}/MC^{Kloe}_{IB}$: we fill our histograms with the KLOE reconstructed photon variables, E^*_γ and θ^*_γ, wheighted with the above-mentioned ratio. DE spectrum is generated separately, folding the Monte Carlo generation with the detector resolution and taking into account the selection efficiency.

8 Fit

To count $K^0_{e3\gamma}$ signal events we fit two-dimensional $f_i(E^*_\gamma, \theta^*_\gamma)$ (i=1,2,3,4) Monte Carlo spectra to the data. Actually is possible to measure R only by using the energy spectrum (we do it and the result matches), but in this case there is no sensitivity to test the presence of DE term. In Fig. 22 are shown the four distributions used as inputs in the fit: IB signal, DE signal, signal-out-of-acceptance ($E^*_\gamma < 30\,\mathrm{MeV}$, $\theta^*_\gamma < 20°$) and background from $K_L \to \pi^+\pi^-\pi^0$ and $K_L \to \pi\mu\nu$.

Looking at the picture we realize that only a simultaneous use of these two variables can disentangle the very low statistic DE component: any projection destroys separation. To check the fit stability as a function of run

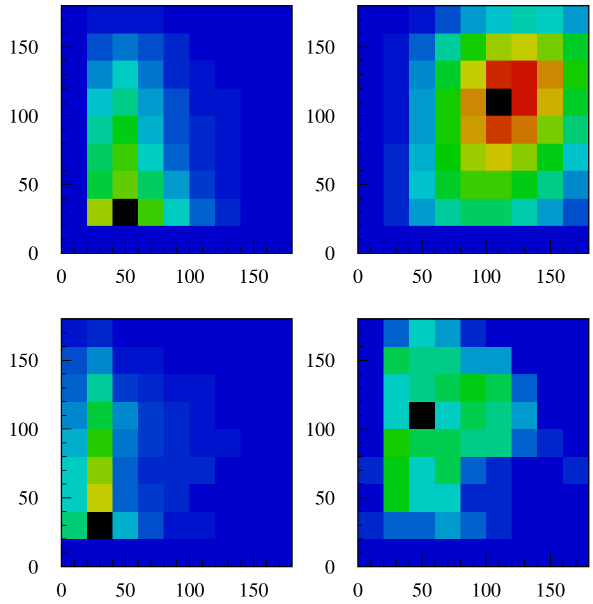

Fig. 22. Monte Carlo distribution, θ^*_γ (deg) *vs* E^*_γ (MeV). From left-top: IB signal, DE signal, signal out-of-acceptance and background. The vertical scale is in arbitrary units.

period we fix the background component, otherwise the fit could not converge (too low background statistic) and we do not use the DE shape (no sensitivity in a single period). The stability is good (Fig. 23). Then we fit all data simultaneously: free parameters of the fit are the population for IB signal, DE signal, signal-out-of-acceptance. We fix the background contribution of $K_L \to \pi^+\pi^-\pi^0$ and $K_L \to \pi\mu\nu$ from Monte Carlo after normalizing to the data entries. As a check we also perform the fit letting all parameters free: the result matches very well but there is a partial loss in statistical precision. For this reason the background fraction is not a free parameter of the fit. The result of the fit and the residual are shown in Fig. 24. The two-dimensional Monte Carlo input shapes are re-arranged into eight $\theta - slices$ uni-dimensional hystograms. Each *slice* covers 20 degrees, from 20° to 180°.

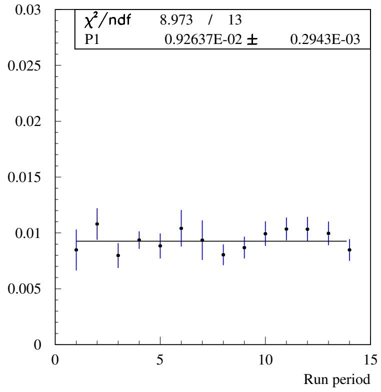

Fig. 23. R result versus run period

The counting result and the correlations of parameters are visible, respec-

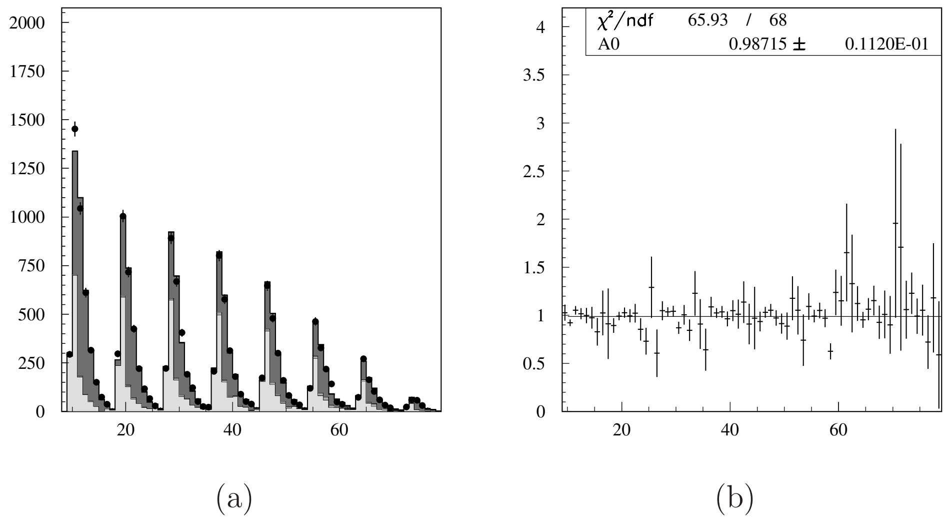

Fig. 24. (a) Fit: dots are data, dark grey is the signal (IB+DE), light grey is the signal-out-of-acceptance; (b) Residual: Fit/Data

tively, in Table 1 and Table 2. The χ^2 is good, giving χ^2/dof=60/69).

	Counting result		
	IB signal	signal-out-acc	DE signal
counting	9083	6726	-102
error	213	194	59

Table 1
Conting from the fit with the statistical error

We normalize our branching ratio measurement to all the inclusive $K^0_{e3(\gamma)}$ events. We get $K^0_{e3(\gamma)}$ events by counting events after TOF selection, background subtraction and efficiency correction. After getting $K^0_{e3\gamma}$ signal from

	Correlation coefficients		
Par	1	2	3
1	1.000	-0.586	-0.254
2		1.000	-0.022
3			1.000

Table 2
Correlation coefficients: 1: IB signal, 2: ke3γ-out-of-acceptance, 3: DE signal

fit counting, taking into account the efficieny, applying the efficiency corrections for tracking, clustering and photon selection, we measure:

$$R = \frac{\mathrm{BR}(K^0_{e3\gamma}; E^*_\gamma > 30\,\mathrm{MeV}, \theta^*_\gamma > 20°)}{\mathrm{BR}(K^0_{e3(\gamma)})} = (924 \pm 23) \times 10^{-5} \qquad (9)$$

Although the χ^2 for the fit is not bad for KLOE Monte Carlo (χ^2/dof = 67/69), the *Kubis* Monte Carlo (χ^2/dof = 60/69) is slightly better. In Fig. 25 is shown the pool when using *Kubis* and Kloe Monte Carlo, giving respectively +0.15 and -0.24.

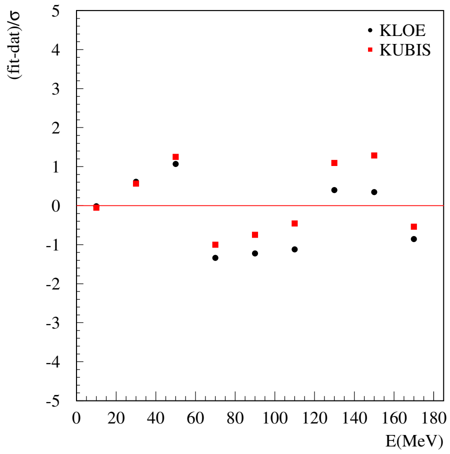

Fig. 25. Fit residual with Kubis and Kloe Monte Carlo.

9 Systematic uncertainties

We estimated all the systematics with the method of cut variations. Tracking, clustering, track-to-cluster association, NV acceptance and analysis cuts all depends on some parameters which define our signal. Any variation on these parameters produces a variation on the result. In the following we report the absolute variation of $10^5\times$ R.

9.1 *Tagging*

We evaluate the systematic uncertainty of the tag efficiency by repeating the measurement using a different tagging alghoritm: we tag K_L requiring K_S alone satisfies the calorimeter trigger with the presence of two clusters from $K_S \to \pi^+\pi^-$ associated with fired trigger sector (*autotrigger*). We observe a change of 4.

9.2 *Tracking*

We evaluate the systematic uncertainties on the tracking efficiency corrections by checking stability of the result when the selection of tracks is modified. The most effective variable in tracking candidates definition is d_c, the distance of closest approach. We vary d_c by a factor of two. We re-evaluate for each different configuration the tracking-efficiency correction, which is run-period dependent. The uncertainty on the tracking efficiency correction is dominated by sample statistics. We observe a change of 1.5

9.3 *Clustering*

As for tracking, we evaluate the systematic uncertainties on the clustering efficiency corrections by checking stability of the result when the TCA association criteria are modified. The most effective variable in the definition of TCA association is the transverse distance, $\mathrm{d}_{\mathrm{tc}\perp}$. We vary the cut on $\mathrm{d}_{\mathrm{tc}\perp}$ from 15 cm to 30 cm, corresponding to a change in efficiency of about 17%. We re-evaluate for each different configuration the clustering efficiency correction, which is run-period dependent. Also in this case the uncertainty on the clustering efficiency corrections is dominated by sample statistics. We observe a change of 5.5 in the result.

9.4 *Kinematic cuts*

We apply loose kinematic cuts. When varying this cut negligible variation for the results are found.

9.5 *Tof cut*

Inclusive $K^0_{e3(\gamma)}$ sample is identified also by using time of flight (TOF). We use a 2-σ cut (see Fig. 5). We vary this cut by 30%. We observe a change of 1.3

9.6 *Momentum mis-calibration and resolution*

The effect of the momentum scale and the momentum resolution have also been considered. We conservatively assume a momentum scale uncertainty

of 0.1%, well above the accuracy obtained with a dedicated analysis [9]. We observe a change of 3 for R.
We also investigate the effect of momentum resolution by changing its value of ± 3%, corresponding to a worst χ^2. The changement on the result is 7.2.

9.7 Fiducial volume

We reduce the fiducial volume by a 20%. This produces a variation on the result of 3.

9.8 Rejection of accidentals

We vary the sliding cut used to remove wrong associations of accidental cluster (see Fig.15). Moving this cut this background vary by a factor of two. This produces a changement in the result of 5.2

9.9 NV acceptance

We search neutral vertex within a well defined sphere. We vary the dimension of its radius by a factor of two. We observe a change of 2.9 in the result.

9.10 Background

In a very conservatively way we remove the cut on Neural Network output: in this way the background level increses almost of a factor of four. We observe a change of 9 for the result.

All systematic errors are summarized in Table 3.

10 R result and DE contribution

Taking into account all systematics the measurements of R yields:

$$R = \frac{\mathrm{BR}(K^0_{e3\gamma}; E^*_\gamma > 30\,\mathrm{MeV}, \theta^*_\gamma > 20^\circ)}{\mathrm{BR}(K^0_{e3(\gamma)})} = (924 \pm 23 \pm 16) \times 10^{-5} \quad (10)$$

From the result on DE it is possible to estimate the $\langle X \rangle$ parameter, defined in the equation 11

$$\frac{d\Gamma}{dE^*_\gamma} = \frac{d\Gamma_{IB}}{dE^*_\gamma} + \langle X \rangle f(E^*_\gamma) \quad (11)$$

As analyzed by the authors of Ref. [2], the structure-dependent contributions can be parametrized in terms of eight structure function V_i and A_i,

Source	$10^5 \times \Delta R$	$\Delta\langle X \rangle$
Tagging	4.0	0.7
Tracking	1.5	0.8
Clustering	5.5	0.1
Kinematic cuts	$\sim$0	$\sim$0
TOF-cut	1.3	0.5
p-miscalibration	3.5	0.2
p-resolution	7.2	0.4
Fiducial volume	3.0	0.5
Rejection acc.	5.2	0.4
NV acceptance	2.9	0.3
BKG Reject.by NN	9.0	0.1
Total	15.5	1.4

Table 3
Summary of the absolute systematic uncertainties on R and $\langle X \rangle$, this last defined in next section

i=1,2,3,4. These terms have been evaluated at $\mathcal{O}(p^6)$ level in ChPT. The dominant contributions are very similar *w.r.t.* the photon energy spectrum. For this reason their effect can be summarized in the so-called *distortion function*, $f(E^*_\gamma)$. The information on the DE term is contained in the effective strength, $\langle X \rangle$, that multiplies $f(E^*_\gamma)$. The autors quote the value

$$\langle X \rangle_{theor} = -1.2 \pm 0.4 \quad \mathcal{O}(p^6) \quad \text{in ChPT} \tag{12}$$

entirely due to the IB-DE interference, as $\mathcal{O}(DE^2)$ term are completely negligible. Starting from counting result for IB and DE, taking into account the difference in the efficiency (IB efficiency is about $\sim$20% higher than DE efficiency), including all systematics we measure

$$\langle X \rangle_{meas} = -2.3 \pm 1.3 \pm 1.4 \tag{13}$$

in agreement with $\mathcal{O}(p^6)$ evaluation. The systematics on $\langle X \rangle$ are evaluated as for R, *i.e.* with the cut variation method. The different contributions are listed in Table 3. The presence of DE contribution reduces the value of R of about 1%. The correlation between R and $\langle X \rangle$, including also systematics, is 3.9%.

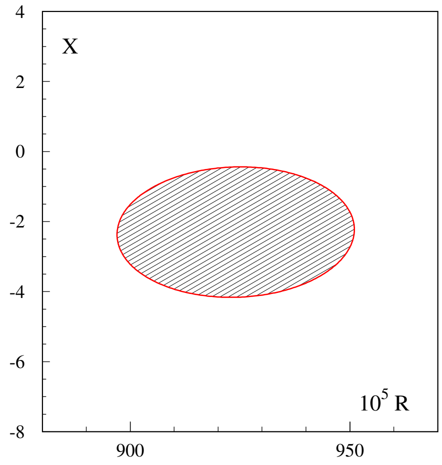

Fig. 26. 1-σ confidence level for R and $\langle X \rangle$ measurement

11 Comparison with the 2001 KTeV measurement

We wish now to make a comparison with the KTeV 2001 measurement of Direct Emission [10]. KTeV Monte Carlo is based on the FFS model [11], a fenomenological model which allows to evaluate the squared matrix element for IB and DE photon emission in $K^0_{e3\gamma}$. In particular, after fitting the data, the foundamental parameters of the model (A, B, C and D), can be extracted. They fit the data with the Monte Carlo photon spectrum, but the available statistic ($\sim$ 15000 signal events) does not allow to have the necessary sensitivity. So they work in the *soft kaon approximation*, *i.e.*, $A = B = 0$. The result of their fit is

$$C = -5 \pm 10 \qquad \text{and} \qquad D = 5^{+19}_{-21}$$

In order to compare theoretical prediction of $\mathcal{O}(p^6)$ ChPT with KTeV result J. Gasser [2] related the $\langle X \rangle$ parameter to the parameters of the FFS model, obtaining:

$$\langle X \rangle = \underbrace{1.4\langle A \rangle}_{-1.9} + \underbrace{0.4\langle B \rangle}_{+\,0.1} + \underbrace{\langle C \rangle}_{+\,0.1} + \underbrace{0.4\langle D \rangle}_{-\,0.1} + \underbrace{1.5\ M_K^2\ \dot{f}_+(0)}_{+\,0.6} = -1.2$$

Hence, the soft kaon approximation hypothesis, having neglected the largest term, *i.e.* $1.4\langle A \rangle$, does not allow one to infer conclusion on the $\langle X \rangle$ parameter.

12 Conclusion

Two different components contribute to the photon emission, the inner bremsstrahlung and the direct emission. The latter describes photon radiation from intermediate hadronic states, giving in this way new information on the hadronic structure. Using E^*_γ and θ^*_γ variables KLOE measured the branching ratio of radiative $K^0_{e3\gamma}$ with respect to the inclusive $K^0_{e3(\gamma)}$. The DE emission contribution comes out from the interference with IB, resulting in a nonzero effective strength, $\langle X \rangle$. KLOE measurement of $\langle X \rangle$ is the first indication of a nonzero Direct Emission contribution in $K^0_{e3\gamma}$ process, also if at 1.2σ significance level. Using the all KLOE data sample will allow to increase the statistic by a facor of 5. This could confirm at $\sim 3\sigma$ significance level the presence of DE and will improve the accuracy on R measurement. In fact, at this stage, the KLOE measurement of R (3% accuracy) is not sufficient to solve the experimental disagreement with theory [2], as shown in Fig. 27

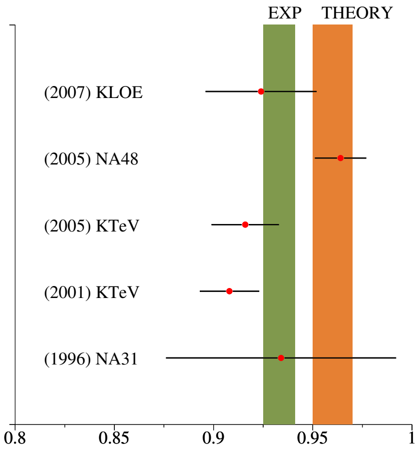

Fig. 27. Recent measurements of R with the standard cut

13 Acknowledgements

We wish to thank Bastian Kubis, one of the authors of Ref. [2], for their indispensable support in providing the Monte Carlo code generator used in this analysis.

References

[1] M. Doncel, Phys. Lett. B 32 (1970) 623.

[2] J. Gasser, et al., Eur. Phys. J. C 40 (2005) 205.

[3] M. Adinolfi, et al., The tracking detector of the KLOE experiment, Nucl. Instrum. Meth. A 488 (2002) 51.

[4] M. Adinolfi, et al., The KLOE electromagnetic calorimeter, Nucl. Instrum. Meth. A 482 (2002) 364.

[5] M. Adinolfi, et al., The trigger system of the KLOE experiment, Nucl. Instrum. Meth. A 492 (2002) 134.

[6] T. Spadaro, C. Gatti, Measurement of the branching fraction and the charge asymmetyry for the decay BR($K_S \to \pi e \nu$) KLOE Note 208.
URL http://www.lnf.infn.it/kloe/pub/knote/kn208.ps

[7] M. Antonelli, P. Beltrame, M. Dreucci, M. Moulson, M. Paultan, A. Sibidanov, Measurements of the absolute branching ratios for dominant K_L decays, the K_L lifetime, and v_{us} with the kloe detector, KLOE Note 204 (2005).
URL http://www.lnf.infn.it/kloe/pub/knote/kn204.ps.gz

[8] C. Gatti, Monte carlo simulation for radiative kaon decays, Eur. Phys. J. C 45 (2006) 417.

[9] A. Antonelli, et al., The KLOE field map revisited, KLOE Memo 233 (2001).

[10] A. Alavi-Harati, et al., Phys. Rev. D 64 (2001) 112004.

[11] H. Fearing, et al., Phys. Rev. D 2 (1970) 542.